ACS OMEGA

http://pubs.acs.org/journal/acsodf

Article

Transition Metal Ions in Methylammonium Chloride Perovskites

Chih Shan Tan*

Cite This: *ACS Omega* 2022, 7, 1412−1419

Read Online

ACCESS | Metrics & More | Article Recommendations | Supporting Information

ABSTRACT: Organic−inorganic perovskite materials have become star materials for future wide band gap optoelectronics due to their excellent optical and electrical properties. However, the lead ions inside perovskites have become a crucial environmental issue in the commercialization of wide band gap perovskite devices . This research tries to find the structure and properties of lead-free perovskite materials by screening Sn^{2+} and transition-metal ions to replace Pb^{2+} within the methylammonium (MA)-based chloride perovskite and find out a new two-dimensional structure of MA-based transition-metal ion chlorides. Overall, $MAZnCl_3$ may be a potential ultraviolet-C luminescent material with a stable two-dimensional structure with a wide band gap of 5.64 eV, which is suitable for ultraviolet-C luminescence applications.

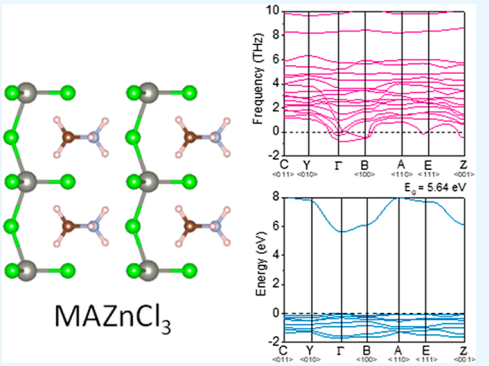

INTRODUCTION

Organic−inorganic perovskite materials have advantages such as high flexibility and low formation temperature and are therefore suitable for wide band gap optoelectronics.[1−4] With the probability of pandemic outbreaks increasing year by year,[5,6] research on convenient disinfection methods[7−10] and wide band gap devices and related materials deserves more attention. Due to their environmentally friendly nature and wide band gap applications, lead-free,[11−13] two-dimensional[14−17] perovskites merit more attention and investigation. Indeed, many transition metals are listed in the periodic table with the same positive divalent ion as Pb^{2+}, making researchers doubt their possibilities. In the past, the Goldschmidt tolerance factor was a primary perovskite method to identify the possible cation according to the ionic radius. The value of the Goldschmidt tolerance factor of the structures should be between 0.85 and 1, so that the perovskite could remain in the cubic system, or deformation might happen.[18,19] However, the fine details of the possible structures and properties of the transition-metal ion perovskite need to be entirely investigated for the deformation of perovskite. The possible transition-metal ion perovskite could be revealed by the density functional theory calculation and the data of lead-free perovskite.

The structure or geometry optimization calculation of density functional theory is well known for estimating the possible crystal structures of unknown crystals and offering detailed information of the stable atom positions. Therefore, the DFT calculation is suitable for investigating the related electron[20−23] and phonon[24−26] properties from an optimized structure. This research figures out the phonon and electron properties of the unknown transition metals in methylammonium (MA) perovskite, with the halide set as chloride, through DFT, and elucidates the detailed information of crystals.

The phonon dispersion diagram and band structure were calculated to identify the optimized transition-metal ion perovskite structures with MA), stability, and semiconductor properties. Here, MA-based perovskites are chosen because of their better structure stability compared to the cesium (Cs^+) and formamidinium (FA^+) ions. The phonon dispersion diagram can reveal the dynamic crystal stability according to the number of imaginary phonon states, and dynamic stability relates to the phase stability. $MAPbCl_3$, $Pm\bar{3}m$, is a wide band gap perovskite (thin film with 3.17 eV[27]) with relatively stable property,[28,29] and the crystal template of this research uses MA-based chloride perovskites for the screening of transition-metal ions. Sn^{2+} and the stable same oxidation state ions of Pb^{2+} (such as Cd^{2+}, Ni^{2+}, Cu^{2+}, Hg^{2+}, Fe^{2+}, Zn^{2+}, Mn^{2+}, and Co^{2+}) were screened by this research.

RESULTS AND DISCUSSION

The optimized structures of $MAPbCl_3$, $MASnCl_3$, and transition-metal ion perovskites, with the same stable oxidation state as that of the lead ion ($MACdCl_3$, $MANiCl_3$, $MACuCl_3$, $MAHgCl_3$, $MAFeCl_3$, $MAZnCl_3$, $MAMnCl_3$, and $MACoCl_3$), are shown in Figure 1a−j. The diameter difference of different cations deforms the $Pm\bar{3}m$ structure of the $MAPbCl_3$ template shown in Figure 1a, and forms two-dimensional materials shown in Figure 1b ($MASnCl_3$), Figure 1d ($MANiCl_3$), Figure 1e

Received: October 31, 2021
Accepted: December 14, 2021
Published: December 28, 2021

https://doi.org/10.1021/acsomega.1c06088
ACS Omega 2022, 7, 1412−1419

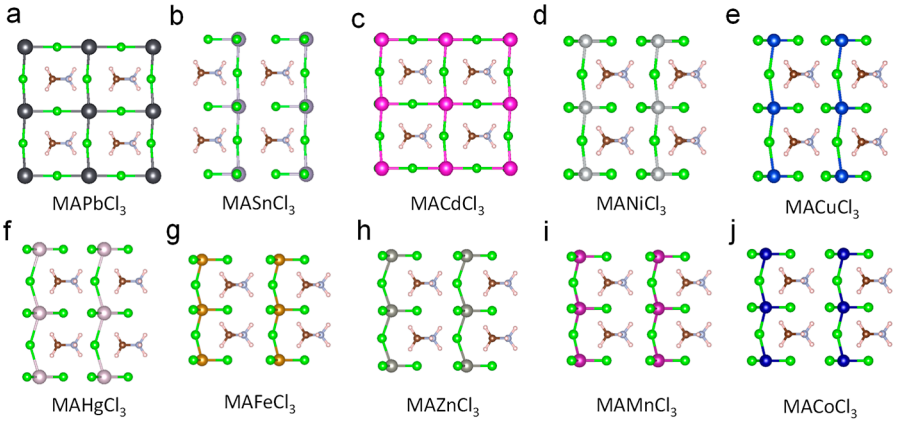

Figure 1. Optimized structures of $MAPbCl_3$ ($Pm\bar{3}m$) and the transition cation replacing structures (a) $MAPbCl_3$, (b) $MASnCl_3$, (c) $MACdCl_3$, (d) $MANiCl_3$, (e) $MACuCl_3$, (f) $MAHgCl_3$, (g) $MAFeCl_3$, (h) $MAZnCl_3$, (i) $MAMnCl_3$, and (j) $MACoCl_3$.

Table 1. Geometry-Optimized Crystal Parameters of the Structures given in Figure 1

Cell parameters	$MAPbCl_3$	$MASnCl_3$	$MACdCl_3$	$MANiCl_3$	$MACuCl_3$	$MAHgCl_3$	$MAFeCl_3$	$MAZnCl_3$	$MAMnCl_3$	$MACoCl_3$
a (Å)	5.75	5.70	5.40	5.30	5.17	5.51	6.36	6.20	6.28	6.21
b (Å)	5.76	5.65	5.40	4.85	5.15	5.43	4.13	4.53	4.14	4.25
c (Å)	5.86	5.90	5.65	6.04	5.50	5.76	6.32	6.21	6.32	6.22
alpha (°)	90.00	90.00	90.00	90.00	90.00	90.00	90.00	90.00	90.00	90.00
beta (°)	90.03	88.92	87.88	87.00	86.18	88.61	85.01	86.39	84.98	87.81
gamma (°)	90.00	90.00	90.00	90.00	90.00	90.00	90.00	90.00	90.00	90.00
Volume (Å^3)	194.18	190.10	164.71	155.02	145.92	172.09	165.36	174.19	163.44	164.14
Density (mg/m^3)	2.956	2.246	2.529	2.111	2.298	3.271	1.951	1.943	1.964	1.997

($MACuCl_3$), Figure 1f ($MAHgCl_3$), Figure 1g ($MAFeCl_3$), Figure 1h ($MAZnCl_3$), Figure 1i ($MAMnCl_3$), and Figure 1j ($MACoCl_3$). Only $MACdCl_3$ in Figure 1c can retain the three-dimensional structure. This indicates that the MA molecular structure being too long for the Sn^{2+}, Ni^{2+}, Cu^{2+}, Hg^{2+}, Fe^{2+}, Zn^{2+}, Mn^{2+}, and Co^{2+} ions undergoes deformation by breaking the three-dimensional structures at the (100) crystal plane and slicing the crystal into two-dimensional structures.

The transition-metal ions in perovskites might offer a potential research direction for discovering new 2D materials, and the optimized structure information is listed in Tables 1 and 2. The radius of transition-metal ions is listed in Table 3. Indeed, Pb^{2+} has the largest ionic radius of 1.33 Å (Table 3), compared to the lower ionic radii of Sn^{2+} (1.18 Å), Ni^{2+} (0.69 Å), Cu^{2+} (0.73 Å), Hg^{2+} (1.19 Å), Fe^{2+} (0.61 Å), Zn^{2+} (0.74 Å), Mn^{2+} (0.67 Å), and Co^{2+} (0.65 Å) cations, and so could not maintain the three-dimensional structures, thereby causing the MA molecule to break and slice the three-dimensional structures at the (100) surface to form two-dimensional structures. The Cd^{2+} ion has a radius of 0.95 Å, different from the radius of Pb^{2+}, so $MACdCl_3$ could retain the three-dimensional structure, as shown in Figure 1c. According to Table 3, the Goldschmidt factor of $MACdCl_3$ is 0.98, the value of a normal three-dimensional structure, whereas the Goldschmidt factor between 0.85 and 1 is for a cubic structure. Therefore, the final structure can endure the MA molecular. This result increases the understanding of the ion replacement of MA-based perovskites and offers more information beyond the Goldschmidt tolerance rule of perovskites. These results could explain that the transition-metal ions could not be suitable doping elements, generally for high-efficiency perovskite solar cells and LED devices.

For MA-based transition-metal ion chlorides, the energy of the crystal system (free energy) is calculated with the same functional as that used for phonons, and the values are listed in Table 3. The free energies of the structures are $MAPbCl_3$ (−64.25 eV), $MASnCl_3$ (−54.22 eV), $MACdCl_3$ (−50.94 eV), $MANiCl_3$ (−53.22 eV), $MACuCl_3$ (−51.57 eV), $MAHgCl_3$ (−48.90 eV), $MAFeCl_3$ (−55.80 eV), $MAZnCl_3$ (−51.60 eV), $MAMnCl_3$ (−56.61 eV), and $MACoCl_3$ (−54.78 eV). $MAPbCl_3$ has the lowest free energy and becomes the most stable crystal in the structures. The dynamic stability of the phonon should identify the phase stability of each crystal. The phonon dispersion diagram and the phonon density of states (DOSs) could identify the dynamic crystal bonding vibration condition and indicate the phase stability. The fewer imaginary phonon states show better dynamic stability of the crystal, and the structure has less possibility to undergo phase transition to another phase. This is due to the bonding vibration within the crystal not giving out energy at a certain point but absorbing the heat energy outside. If suppose the bonding vibration keeps giving out energy at a certain point, then the bonding will break by the vibrational energy loss in a certain direction, and the phase transition happens toward a stabilized bonding arrangement. Phonon dispersion and phonon DOS diagrams of the structures are shown in Figure 2a-j, and the imaginary phonon

https://doi.org/10.1021/acsomega.1c06088
ACS Omega 2022, 7, 1412−1419

Table 2. Geometry-Optimized Atomic Positions of the Structures in Figure 1, from Top to Down—*x*, *y*, and *z*

Atom	$MAPbCl_3$ (X = Pb)	$MASnCl_3$ (X = Sn)	$MACdCl_3$ (X = Cd)	$MANiCl_3$ (X = Ni)	$MACuCl_3$ (X = Cu)	$MAHgCl_3$ (X = Hg)	$MAFeCl_3$ (X = Fe)	$MAZnCl_3$ (X = Zn)	$MAMnCl_3$ (X = Mn)	$MACoCl_3$ (X = Co)
H_1	0.23018 0.35346 0.97941	0.23259 0.35100 0.98065	0.23679 0.34248 0.02046	0.22567 0.32648 0.04663	0.23160 0.33463 0.04312	0.22610 0.34415 0.99210	0.20247 0.30110 0.03434	0.21233 0.31695 0.02028	**0.20593** **0.30169** **0.03509**	0.20796 0.30617 0.00636
H_2	0.81361 0.34386 0.04713	0.81047 0.34109 0.04504	0.78923 0.33311 0.99153	0.77535 0.31398 0.00670	0.77371 0.32446 0.00304	0.78606 0.33452 0.03825	0.81901 0.28398 0.00254	0.81620 0.30304 0.01749	0.81744 0.28447 0.00636	0.81055 0.28962 0.03702
H_3	0.17060 0.50000 0.21735	0.16678 0.50000 0.21660	0.10698 0.50000 0.24704	0.07539 0.50000 0.25947	0.08082 0.50000 0.27700	0.14581 0.50000 0.23212	0.06395 0.50000 0.23872	0.09638 0.50000 0.23451	0.06845 0.50000 0.24039	0.10572 0.50000 0.22856
H_4	0.88098 0.50000 0.79025	0.88631 0.50000 0.79093	0.93455 0.50000 0.74915	0.94182 0.50000 0.78585	0.94568 0.50000 0.75915	0.88205 0.50000 0.78028	0.96035 0.50000 0.78653	0.93888 0.50000 0.78832	0.95819 0.50000 0.78957	0.90729 0.50000 0.79672
X	0.47417 0.00000 0.48451	0.44860 0.00000 0.49532	0.49257 0.00000 0.52209	0.59524 0.00000 0.55321	0.59344 0.00000 0.55976	0.59528 0.00000 0.57451	0.56357 0.00000 0.55452	0.56515 0.00000 0.55810	0.55420 0.00000 0.54164	0.57847 0.00000 0.55812
C	0.89498 0.50000 0.97674	0.89493 0.50000 0.97614	0.89481 0.50000 0.94117	0.88649 0.50000 0.96380	0.88625 0.50000 0.95443	0.87950 0.50000 0.97129	0.91412 0.50000 0.95828	0.90852 0.50000 0.96501	0.91292 0.50000 0.96171	0.89626 0.50000 0.97416
N	0.14502 0.50000 0.04117	0.14542 0.50000 0.04210	0.13064 0.50000 0.06385	0.11646 0.50000 0.09004	0.12091 0.50000 0.09031	0.13137 0.50000 0.05175	0.10480 0.50000 0.07590	0.11687 0.50000 0.06708	0.10751 0.50000 0.07729	0.11518 0.50000 0.06095
Cl_1	0.42701 0.00000 0.97456	0.42269 0.00000 0.94624	0.43956 0.00000 0.98128	0.36417 0.00000 0.85096	0.36159 0.00000 0.89000	0.40356 0.00000 0.95222	0.45181 0.00000 0.89200	0.44963 0.00000 0.90872	0.45404 0.00000 0.88852	0.43142 0.00000 0.89103
Cl_2	0.42784 0.50000 0.51756	0.42871 0.50000 0.51415	0.45753 0.50000 0.51036	0.54549 0.50000 0.50149	0.52478 0.50000 0.51272	0.45124 0.50000 0.51214	0.48168 0.50000 0.47276	0.44056 0.50000 0.46140	0.47668 0.50000 0.46618	0.50623 0.50000 0.47596
Cl_3	0.97018 0.00000 0.44018	0.99881 0.00000 0.46254	0.96968 0.00000 0.45647	0.95125 0.00000 0.38394	0.95428 0.00000 0.35969	0.96521 0.00000 0.36040	0.89509 0.00000 0.44293	0.90532 0.00000 0.43672	0.89963 0.00000 0.44719	0.90075 0.00000 0.42313

Table 3. Metal Ion Radius, Energy of the System (E_0), Imaginary Part of Phonon DOS, and Debye Temperature (Θ_D) of Different Structures

	Metal ion radius (Å)	Goldschmidt factor	Energy of the system, E_0 (eV)	Imaginary part of phonon DOS (%)	Debye temperature, θ_D (K)
$MAPbCl_3$	1.33	0.90	-64.25	1.78	102
$MASnCl_3$	0.83	1.08	-54.22	3.09	106
$MACdCl_3$	1.09	0.98	-50.94	2.79	131
$MANiCl_3$	0.83	1.08	-53.22	14.63	173
$MACuCl_3$	0.87	1.07	-51.57	6.64	134
$MAHgCl_3$	1.16	0.96	-48.90	3.44	93
$MAFeCl_3$	0.75	1.12	-55.80	4.32	144
$MAZnCl_3$	0.88	1.06	-51.60	0.97	106
$MAMnCl_3$	0.81	1.09	-56.61	10.94	161
$MACoCl_3$	0.79	1.10	-54.78	2.20	123

density of states (DOS) of the structures are listed in Table 3. Here, the imaginary part of phonon DOS, by counting the portion of imaginary phonon DOS in the whole phonon states, is used for the whole dynamic structure consideration. The Goldschmidt factors are also listed in Table 3 according to the radius of the MA^+ cation as 2.62 Å and the Cl^- anion as 1.67 Å.

For two-dimensional MA-based transition-metal ion chlorides, $MANiCl_3$ (Figure 2d) and $MAMnCl_3$ (Figure 2i) might be the two most dynamic unstable structures, with abundant imaginary phonon states. Indeed, the imaginary part of phonon DOS is listed in Table 3, and the values of $MANiCl_3$ and $MAMnCl_3$ are 14.63 and 10.94%, respectively. Even though $MACdCl_3$ has the three-dimensional structure, as shown in Figure 1c, 2.79% of imaginary phonon DOS indicates that the unstable dynamic conduction might decompose eventually. Two-dimensional $MAZnCl_3$ has 0.97% imaginary part of phonon DOS, lower than that of $MAPbCl_3$ (1.78%), as presented in Table 3, indicating that $MAZnCl_3$ has better dynamic structural stability and has the potential for the device application. The temperature-dependent diagram in Figure 2k is calculated as the same functional as phonon and used to find out the Debye temperature of each crystal. For a solid-state material, the Debye temperature has a square mathematical relationship

https://doi.org/10.1021/acsomega.1c06088
ACS Omega 2022, 7, 1412−1419

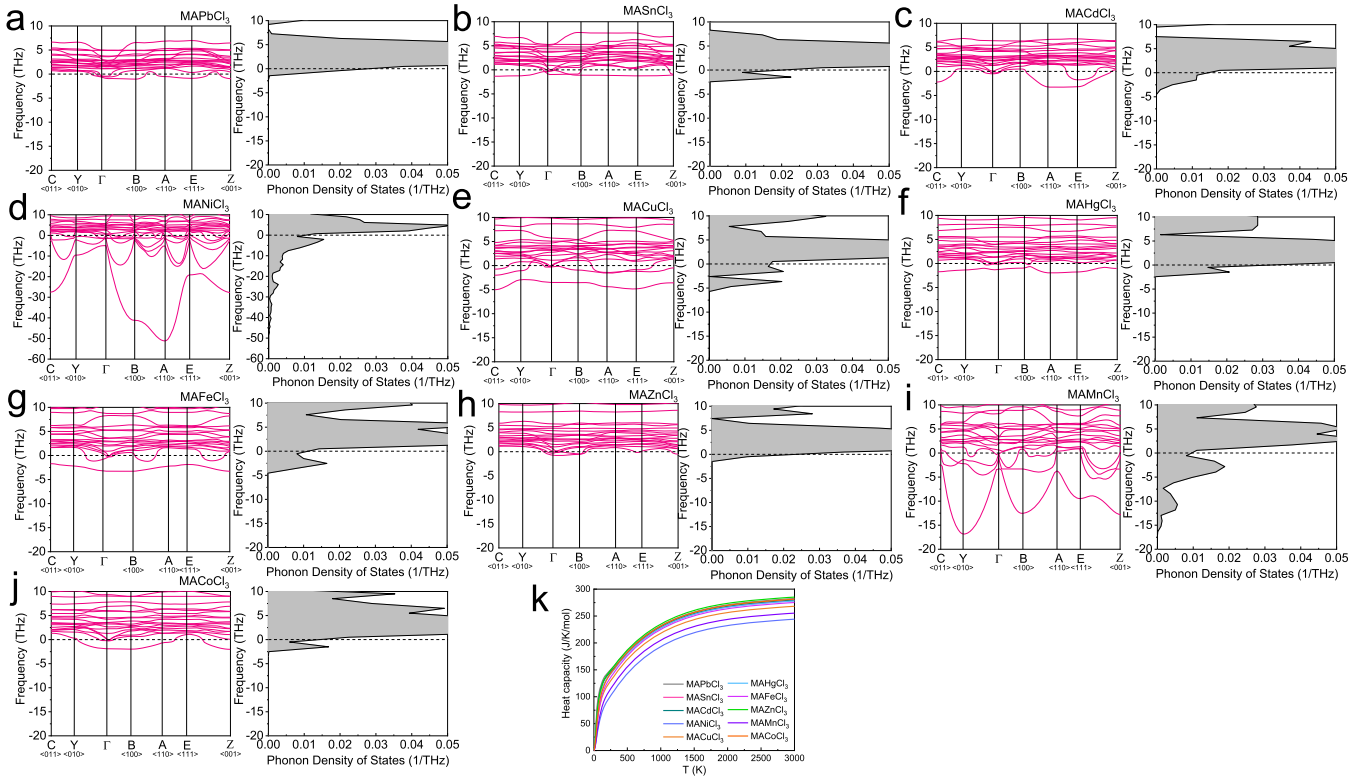

Figure 2. Phonon dispersion, phonon density of states, and temperature-dependent heat capacity diagrams of the structures. (a) $MAPbCl_3$, (b) $MASnCl_3$, (c) $MACdCl_3$, (d) $MANiCl_3$, (e) $MACuCl_3$, (f) $MAHgCl_3$, (g) $MAFeCl_3$, (h) $MAZnCl_3$, (i) $MAMnCl_3$ (j) $MACoCl_3$ and (k) temperature-dependent heat capacity diagram of the structures.

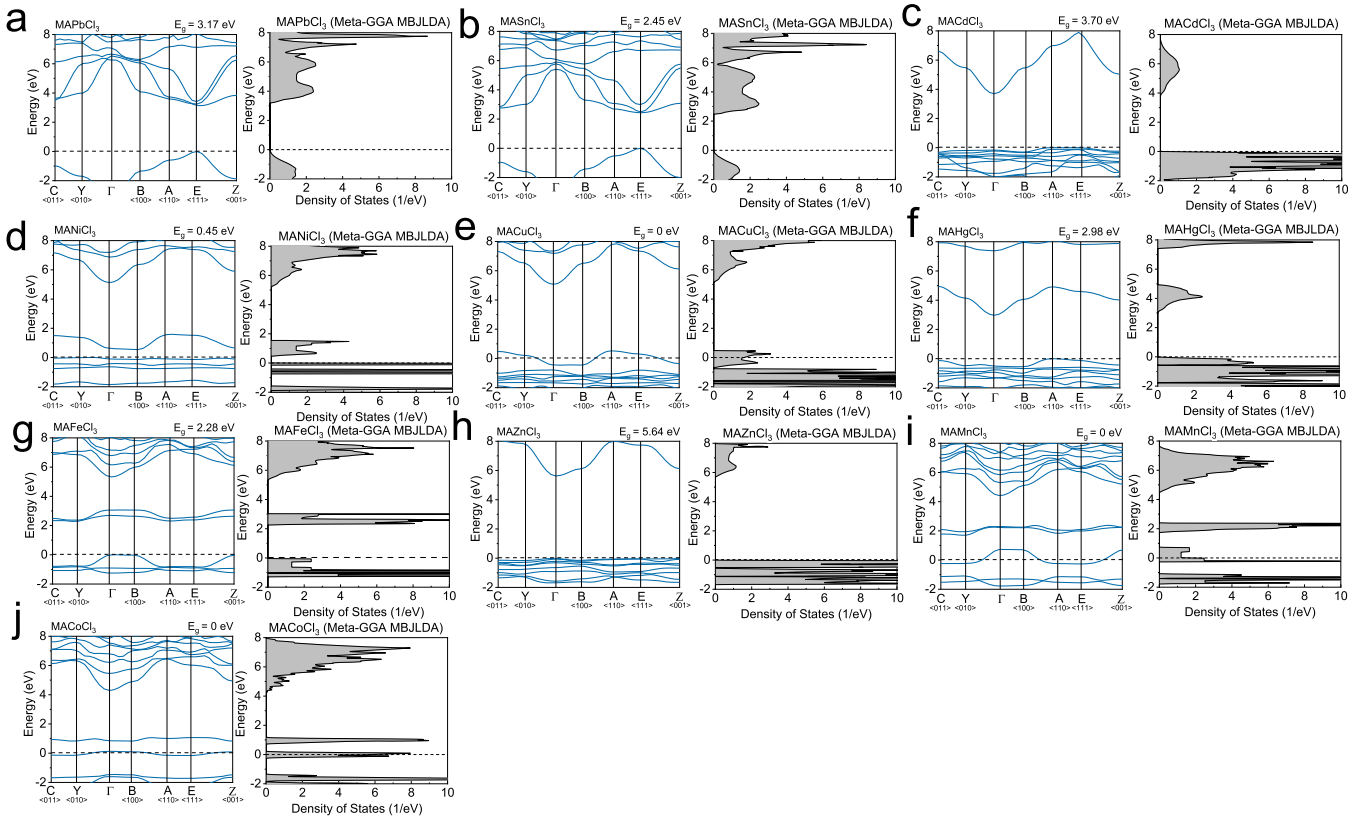

Figure 3. Band structure and density of states of the structures. (a) $MAPbCl_3$, (b) $MASnCl_3$, (c) $MACdCl_3$, (d) $MANiCl_3$, (e) $MACuCl_3$, (f) $MAHgCl_3$, (g) $MAFeCl_3$, (h) $MAZnCl_3$, (i) $MAMnCl_3$, and (j) $MACoCl_3$.

https://doi.org/10.1021/acsomega.1c06088
ACS Omega 2022, 7, 1412−1419

with the melting temperature, and a higher Debye temperature might accompany a higher melting temperature.

Furthermore, a higher melting temperature is accompanied by a higher phase formation temperature, and the Debye temperature calculation could offer the essential estimation of the crystal formation temperature. The Debye temperatures (Θ_D) of each structure are $MAPbCl_3$ (Θ_D = 102 K), $MASnCl_3$ (Θ_D = 106 K), $MACdCl_3$ (Θ_D = 131 K), $MANiCl_3$ (Θ_D = 173 K), $MACuCl_3$ (Θ_D = 134 K), $MAHgCl_3$ (Θ_D = 93 K), $MAFeCl_3$ (Θ_D = 144 K), $MAZnCl_3$ (Θ_D = 106 K), $MAMnCl_3$ (Θ_D = 161 K), and $MACoCl_3$ (Θ_D = 123 K), which are listed in Table 3. The 2D $MAZnCl_3$ structure, with comparable dynamic stable property, has a Debye temperature (106 K) nearly the same value as $MAPbCl_3$ (102 K). In addition, the slight difference in the Debye temperature between $MAZnCl_3$ and $MAPbCl_3$ reveals that $MAZnCl_3$ could be synthesized at the same temperature as $MAPbCl_3$. The information could be helpful for future $MAZnCl_3$ device applications.

The band structures and densities of states (DOSs) of $MAPbCl_3$, $MASnCl_3$, and transition-metal ion MA chlorides are shown in Figure 3, and the exchange−correlation functional of DFT is chosen as meta-GGA-MBJLDA. It is not only that meta-GGA-MBJLDA needs less expensive computational requirement with an accuracy similar to those of hybrid functionals or GW methods but also that the calculation result of $MAPbCl_3$ by meta-GGA-MBJLDA is 3.17 eV, as shown in Figure 3a, which is the same as the $MAPbCl_3$ thin-film experimental value of 3.17 eV.[27] Therefore, meta-GGA-MBJLDA is a suitable exchange−correlation functional of DFT for screening and estimating the band structures of $MASnCl_3$, and the chemical composition of transition-metal ion MA chloride is similar to that of $MAPbCl_3$. Figure 3 shows the DFT band structures of $MAPbCl_3$ (E_g = 3.17 eV, direct), $MASnCl_3$ (E_g = 2.45 eV, direct), $MACdCl_3$ (E_g = 3.70 eV, indirect), $MANiCl_3$ (E_g = 0.45 eV, indirect), $MACuCl_3$ (E_g = 0 eV), $MAHgCl_3$ (E_g = 2.98 eV, indirect), $MAFeCl_3$ (E_g = 2.28 eV, indirect), $MAZnCl_3$ (E_g = 5.64 eV, direct), $MAMnCl_3$ (E_g = 0 eV), and $MACoCl_3$ (E_g = 0 eV). For $MACuCl_3$, $MAMnCl_3$, and $MACoCl_3$ shown in Figure 3e,i,j, bands cross the Fermi level, and the electron can easily move up and down across the Fermi level. The three structures have semimetal-like band structures, and even using a different functional, GGAPBEsol, the three structures still have the same semimetal band structures, as shown in Figure S1e,i,j.

In Figure 3b,f,g, the Sn^{2+}, Hg^{2+}, and Fe^{2+} ion replacements of the Pb^{2+} ion will reduce the band gap, even though Hg^{2+} is not environmentally friendly, and the Sn^{2+} and Fe^{2+} ions could be good candidates for reducing the perovskite band gap in future two-dimensional optoelectronic device applications. In Figure 3c, the three-dimensional $MACdCl_3$ structure has a slightly wider band gap of 3.70 eV, indicating that the Cd^{2+} cation replaces Pb^{2+} within MA-based perovskites, which might increase the band gap. In Figure 3d, two-dimensional $MANiCl_3$ has a 0.45 eV band gap with a near-infrared range spectrum, emitting 2756 nm wavelength as an indirect band gap. The ultrasmall band gap might be due to the isolated low conduction band structure above the Fermi level. This research might find a near-infrared material during 2D perovskite material screening and indicated that $MANiCl_3$ could be used for making the near-infrared detector device. The two-dimensional structures of $MACuCl_3$, $MAMnCl_3$, and $MACoCl_3$ have zero band gap, exhibiting metal-like properties, as shown in Figure 3e,i,j. The DOS diagrams in Figure 3e,i,j also show many states crossing the Fermi levels for $MACuCl_3$, $MAMnCl_3$, and $MACoCl_3$, and the crossing bunch of states at the Fermi level are interesting electrical structures. It is a kind of bridge between the electron and hole states, exhibiting metal-like properties. Finally, $MAZnCl_3$ might be the good predictable ultraviolet-C luminescent material with a wide direct band gap, 5.64 eV, at the gamma point, as shown in Figure 2h. Table 4 lists the detailed band structure information, and N/A means no electron transition between the valence and conduction bands in two-dimensional $MACuCl_3$, $MAMnCl_3$, and $MACoCl_3$. Due to the uncommon ultrawide band gap and near-infrared properties, the electrical properties and stabilities of two-dimensional $MAZnCl_3$ and $MANiCl_3$ need to be investigated further for ultraviolet-C and near-infrared device reference.

Table 4. Photon Behavior of the Structures in Figure 3

	Carrier transfer (VB_{max} to CB_{min})	Band gap (eV/nm)
$MAPbCl_3$	<111> to <111>	3.17/391
$MASnCl_3$	<111> to <111>	2.45/506
$MACdCl_3$	<110> to <000>	3.70/335
$MANiCl_3$	<000> to <100>	0.45/2756
$MACuCl_3$	N/A	0
$MAHgCl_3$	<000> to <110>	2.98/416
$MAFeCl_3$	<000> to <000>	2.28/544
$MAZnCl_3$	<111> to <000>	5.64/220
$MAMnCl_3$	N/A	0
$MACoCl_3$	N/A	0

The whole temperature range of temperature-dependent electrical conductivity and carrier mobility of the structures is shown in Figure 4a−c. The calculation is performed by the GGA-PBEsol exchange−correlation functional in DFT. The optimum device working temperature is found to be in the range of 280−380 K, as shown in Figure 4d−f. The electrical conductivity and carrier mobility values are listed in Tables 5 and 6. The experimental electrical conductivity and carrier mobility of thin-film $MAPbCl_3$ are 1.8×10^{-6} (Ω^{-1} m^{-1}) and 4.14 (cm^2 V^{-1} S^{-1}),[30] respectively, and the calculation results from this research of $MAPbCl_3$ are 1.22×10^{-6} (Ω^{-1} m^{-1}) and 3.1322 (cm^2 V^{-1} S^{-1}), listed in Tables 5 and 6. The experimental measurements of electrical conductivity and carrier mobility of $MAPbCl_3$ are conducted at room temperature, and the material screening calculation is set at room temperature. Therefore, the calculation result of $MAPbCl_3$ is similar to the experimental measurement result and offers a relatively referable value of electrical conductivity and carrier mobility for the unknown perovskite-related structure screening. In Figure 4a, $MACuCl_3$, $MAMnCl_3$, and $MACoCl_3$ have higher temperature-dependent electrical conductivities than other screening materials, around 10 000 to 100 times, and need a separate demonstration. In Figure 4b, the whole temperature ranges of temperature-dependent electrical conductivity of the semiconductor ranges, such as $MAPbCl_3$, $MASnCl_3$, $MACdCl_3$, $MANiCl_3$, $MAHgCl_3$, $MAFeCl_3$, and $MAZnCl_3$, are shown. Indeed, the electrical conductivities of semiconductors will increase with the increase in temperature, and the carrier mobility values show a direct value jump when the temperature is higher than the activation temperature, and different screening materials have different activation temperatures. However, the whole temperature range diagram of electrical conductivities and carrier mobilities is not

https://doi.org/10.1021/acsomega.1c06088
ACS Omega 2022, 7, 1412−1419

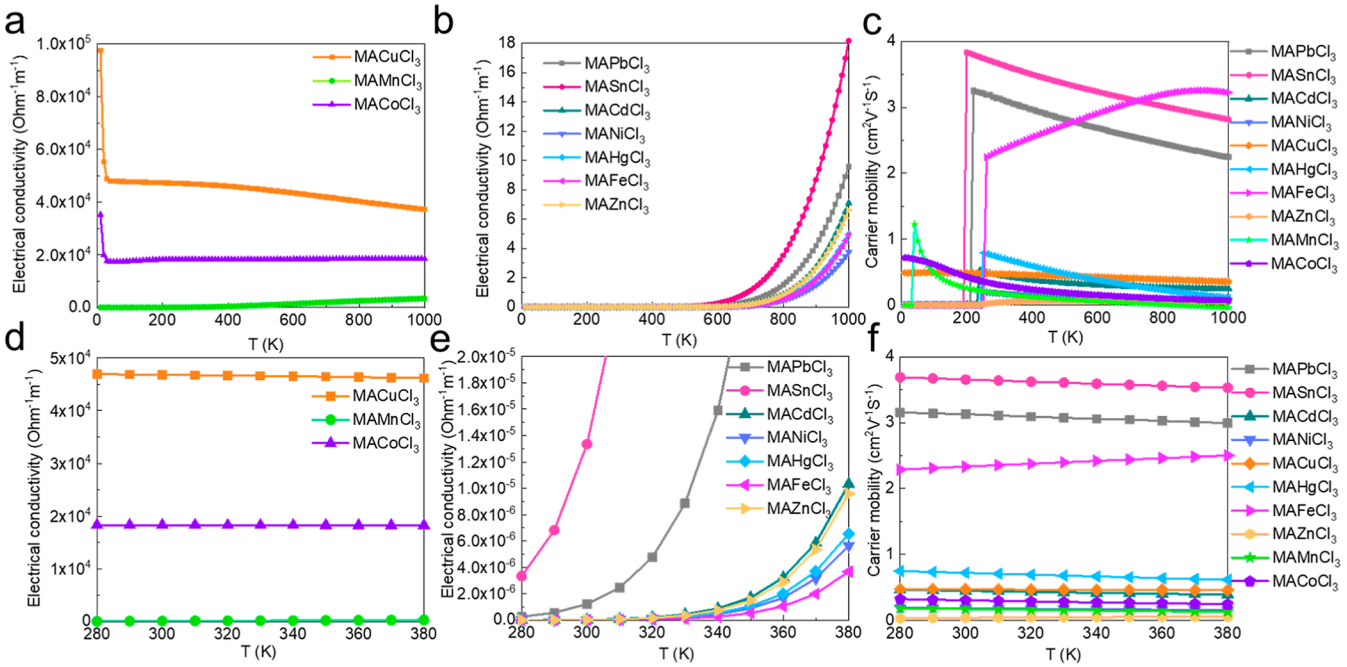

Figure 4. Temperature-dependent electrical conductivity and carrier mobility of $MaPbCl_3$ and transition cations replacing structures. Temperature-dependent electrical conductivities (0−1000 K) of (a) $MACuCl_3$, $MAMnCl_3$, and $MACoCl_3$ and (b) $MAPbCl_3$, $MASnCl_3$, $MACdCl_3$, $MANiCl_3$, $MAHgCl_3$, $MAFeCl_3$, and $MAZnCl_3$. (c) Temperature-dependent carrier densities (0−1000 K) of $MaPbCl_3$ and transition cations replacing structures. The device working temperature range and temperature-dependent electrical conductivities of (d) $MACuCl_3$, $MAMnCl_3$, and $MACoCl_3$ and (e) $MAPbCl_3$, $MASnCl_3$, $MACdCl_3$, $MANiCl_3$, $MAHgCl_3$, $MAFeCl_3$, and $MAZnCl_3$. (f) Temperature-dependent carrier densities (280−380 K) of $MaPbCl_3$ and transition cations replacing structures.

Table 5. Temperature-dependent Electrical Conductivity of the Structures in Figure 4d,e

T (K)	$MAPbCl_3$ ($\Omega^{-1}m^{-1}$)	$MASnCl_3$ ($\Omega^{-1}m^{-1}$)	$MACdCl_3$ ($\Omega^{-1}m^{-1}$)	$MANiCl_3$ ($\Omega^{-1}m^{-1}$)	$MACuCl_3$ ($\Omega^{-1}m^{-1}$)	$MAHgCl_3$ ($\Omega^{-1}m^{-1}$)	$MAFeCl_3$ ($\Omega^{-1}m^{-1}$)	$MAZnCl_3$ ($\Omega^{-1}m^{-1}$)	$MAMnCl_3$ ($\Omega^{-1}m^{-1}$)	$MACoCl_3$ ($\Omega^{-1}m^{-1}$)
280	2.57 x 10^{-7}	3.32 x 10^{-6}	6.14 x 10^{-9}	2.51 x 10^{-9}	4.69 x 10^{4}	3.43 x 10^{-9}	1.26 x 10^{-9}	4.26 x 10^{-9}	76.59	1.83 x 10^{4}
290	5.74 x 10^{-7}	6.81 x 10^{-6}	1.61 x 10^{-8}	6.91 x 10^{-9}	4.68 x 10^{4}	9.17 x 10^{-9}	3.56 x 10^{-9}	1.17 x 10^{-8}	92.34	1.83 x 10^{4}
300	1.22 x 10^{-6}	1.33 x 10^{-5}	3.98 x 10^{-8}	1.78 x 10^{-8}	4.68 x 10^{4}	2.30 x 10^{-8}	9.42 x 10^{-9}	3.01 x 10^{-8}	110.00	1.83 x 10^{4}
310	2.46 x 10^{-6}	2.50 x 10^{-5}	9.29 x 10^{-8}	4.29 x 10^{-8}	4.67 x 10^{4}	5.44 x 10^{-8}	2.34 x 10^{-8}	7.27 x 10^{-8}	129.62	1.83 x 10^{4}
320	4.76 x 10^{-6}	4.51 x 10^{-5}	2.06 x 10^{-7}	9.83 x 10^{-8}	4.66 x 10^{4}	1.22 x 10^{-7}	5.51 x 10^{-8}	1.66 x 10^{-7}	151.23	1.83 x 10^{4}
330	8.86 x 10^{-6}	7.84 x 10^{-5}	4.35 x 10^{-7}	2.14 x 10^{-7}	4.66 x 10^{4}	2.62 x 10^{-7}	1.23 x 10^{-7}	3.62 x 10^{-7}	174.85	1.83 x 10^{4}
340	1.59 x 10^{-5}	1.32 x 10^{-4}	8.81 x 10^{-7}	4.45 x 10^{-7}	4.65 x 10^{4}	5.37 x 10^{-7}	2.62 x 10^{-7}	7.53 x 10^{-7}	200.47	1.83 x 10^{4}
350	2.77 x 10^{-5}	2.16 x 10^{-4}	1.72 x 10^{-6}	8.87 x 10^{-7}	4.64 x 10^{4}	1.05 x 10^{-6}	5.36 x 10^{-7}	1.50 x 10^{-6}	228.09	1.83 x 10^{4}
360	4.67 x 10^{-5}	3.45 x 10^{-4}	3.22 x 10^{-6}	1.70 x 10^{-6}	4.64 x 10^{4}	2.01 x 10^{-6}	1.05 x 10^{-6}	2.88 x 10^{-6}	257.69	1.83 x 10^{4}
370	7.66 x 10^{-5}	5.36 x 10^{-4}	5.86 x 10^{-6}	3.15 x 10^{-6}	4.63 x 10^{4}	3.68 x 10^{-6}	2.00 x 10^{-6}	5.34 x 10^{-6}	289.24	1.83 x 10^{4}
380	1.23 x 10^{-4}	8.15 x 10^{-4}	1.03 x 10^{-5}	5.65 x 10^{-6}	4.62 x 10^{4}	6.55 x 10^{-6}	3.67 x 10^{-6}	9.60 x 10^{-6}	322.68	1.83 x 10^{4}

easy to compare. In Table 5, two-dimensional $MACuCl_3$ and $MACoCl_3$ have the highest two electrical conductivities as 4.68 × 10^4 (Ω^{-1} m^{-1}) and 1.83 × 10^4 (Ω^{-1} m^{-1}) at room temperature, much higher than the typical semiconductors. As a result, two-dimensional $MAMnCl_3$ has an electrical conductivity of 110 (Ω^{-1} m^{-1}) at room temperature, higher than the standard semiconductor value. For the potential ultraviolet-C luminescent material, $MAZnCl_3$ has an electrical conductivity of 3.01 × 10^{-8} (Ω^{-1} m^{-1}) in Table 5, which is lower than that of $MAPbCl_3$, which is 1.22 × 10^{-6} (Ω^{-1} m^{-1}). $MAZnCl_3$ has a carrier mobility of 0.0396 (cm^2 V^{-1} S^{-1}), which is lower than that of $MAPbCl_3$, which is 3.1322 (cm^2 V^{-1} S^{-1}). As a result, the two-dimensional $MAZnCl_3$ is transformed to $MAPbCl_3$, with Zn^{2+} replacing Pb^{2+}, which has a band gap property of 5.64 eV and an luminescence emission wavelength of 220 nm, with an electrical conductivity and a carrier mobility of 3.01 × 10^{-8} (Ω^{-1} m^{-1}) and 0.03961 (cm^2 V^{-1} S^{-1}), respectively.

CONCLUSIONS

In summary, in this research, $MAPbCl_3$ was chosen as a screening template and the Pb^{2+} ion was replaced with Sn^{2+} and transition-metal ions with the same stable oxidation state as Cd^{2+}, Ni^{2+}, Cu^{2+}, Hg^{2+}, Fe^{2+}, Zn^{2+}, Mn^{2+}, and Co^{2+}. The MA molecular became too long under lower ionic radius conditions, and the structures deformed to two-dimensional structures, except $MACdCl_3$. Indeed, the DFT calculation shows that

https://doi.org/10.1021/acsomega.1c06088
ACS Omega 2022, 7, 1412−1419

Table 6. Temperature-dependent Carrier Mobilities of the Structures in Figure 4f

T (K)	$MAPbCl_3$ ($cm^2V^{-1}S^{-1}$)	$MASnCl_3$ ($cm^2V^{-1}S^{-1}$)	$MACdCl_3$ ($cm^2V^{-1}S^{-1}$)	$MANiCl_3$ ($cm^2V^{-1}S^{-1}$)	$MACuCl_3$ ($cm^2V^{-1}S^{-1}$)	$MAHgCl_3$ ($cm^2V^{-1}S^{-1}$)	$MAFeCl_3$ ($cm^2V^{-1}S^{-1}$)	$MAZnCl_3$ ($cm^2V^{-1}S^{-1}$)	$MAMnCl_3$ ($cm^2V^{-1}S^{-1}$)	$MACoCl_3$ ($cm^2V^{-1}S^{-1}$)
280	3.1565	3.6896	0.4689	0.1908	0.4744	0.7472	2.2891	0.0313	0.1884	0.3248
290	3.1396	3.6726	0.4596	0.1874	0.4730	0.7335	2.3122	0.0357	0.1819	0.3151
300	3.1322	3.6558	0.4507	0.1839	0.4715	0.7198	2.3348	0.0396	0.1757	0.3060
310	3.1087	3.6392	0.4422	0.1805	0.4701	0.7062	2.3569	0.0431	0.1698	0.2973
320	3.0910	3.6229	0.4340	0.1770	0.4686	0.6927	2.3786	0.0463	0.1642	0.2890
330	3.0745	3.6067	0.4262	0.1736	0.4671	0.6794	2.3999	0.0491	0.1588	0.2812
340	3.0556	3.5907	0.4187	0.1702	0.4656	0.6661	2.4209	0.0516	0.1536	0.2738
350	3.0458	3.5750	0.4115	0.1669	0.4641	0.6530	2.4416	0.0537	0.1486	0.2667
360	3.0273	3.5594	0.4046	0.1637	0.4626	0.6400	2.4620	0.0556	0.1437	0.2599
370	3.0091	3.5440	0.3980	0.1605	0.4610	0.6272	2.4821	0.0572	0.1391	0.2534
380	2.9948	3.5289	0.3917	0.1574	0.4595	0.6145	2.5020	0.0587	0.1345	0.2472

$MAPbCl_3$ has a band gap of 3.17 eV, with an electrical conductivity of 1.22×10^{-6} (Ω^{-1} m^{-1}) and a carrier mobility of 3.1322 (cm^2 V^{-1} S^{-1}), which are very close to the actual experimental values and show that the calculated values of this study could be taken as the reference. According to the lower imaginary states of two-dimensional $MAZnCl_3$ phonon DOS with an ultra-wide band gap (5.64 eV), $MAZnCl_3$ is a stable structure for future ultraviolet-C luminescence applications. The calculated electrical conductivity and carrier mobility of $MAZnCl_3$ are 3.01×10^{-8} (Ω^{-1} m^{-1}) and 0.0396 (cm^2 V^{-1} S^{-1}), respectively. Finally, this research points out that $MAZnCl_3$ is a stable structure and has the potential for ultraviolet-C optoelectronic applications.

METHODS

The calculations were processed by VASP (Vienna *ab initio* simulation package)[31,32] with different exchange−correlation functionals, GGA-PBEsol[33] and meta-GGA-MBJLDA,[34,35] for determining their semiconductor and thermodynamic properties. After processing, structure optimization was performed for new structures based on the GGA-PBE[36] with 520 eV plane-wave cut-off energy, *k*-spacing with a 5 × 5 × 5 mesh, and first-order Methfessel−Paxton smearing with a width of 0.2 eV. GGA-PBE calculated the phonon behaviors of the atomic models with a plane-wave cut-off energy of 500 eV, *k*-spacing as 5 × 5 × 5 mesh, and a linear tetrahedron method with Bloechl corrections to the energy. For the electronic property (electrical conductivity, carrier mobility, and carrier density) calculations, GGA-PBEsol was set a plane-wave cut-off energy of 400 eV and *k*-spacing with a 3 × 3 × 3 mesh and used with the chemical potential of 12 mu in total 30 mu. For electronic band structure results, meta-GGA-MBJLDA was used with a plane-wave cut-off energy of 500 eV, a *k*-spacing of 3 × 3 × 3 mesh, and a linear tetrahedron method.

ASSOCIATED CONTENT

Supporting Information

The Supporting Information is available free of charge at https://pubs.acs.org/doi/10.1021/acsomega.1c06088.

Additional band structures and temperature-dependent carrier densities (PDF)

AUTHOR INFORMATION

Corresponding Author

Chih Shan Tan − *Institute of Electronics, National Yang Ming Chiao Tung University, Hsinchu 30010, Taiwan;* orcid.org/0000-0001-9043-3237; Email: cstan@nycu.edu.tw

Complete contact information is available at: https://pubs.acs.org/10.1021/acsomega.1c06088

Author Contributions

Chih Shan Tan initiated all the research ideas, performed the calculations, and completed the paper writing independently.

Notes

The author declares no competing financial interest.

ACKNOWLEDGMENTS

This work was funded by the Ministry of Science and Technology of Taiwan (Grants MOST 110-2636-E-009-020).

REFERENCES

(1) Cai, P.; Huang, Y.; Seo, H. J. Anti-Stokes Ultraviolet Luminescence and Exciton Detrapping in the Two-Dimensional Perovskite (C6H5C2H4NH3)2PbCl4. *J. Phys. Chem. Lett.* **2019**, *10*, 4095−4102 Published Online: Jul. 9, 2019.

(2) Tan, C. S.; Hou, Y.; Saidaminov, M. I.; Proppe, A.; Huang, Y. S.; Zhao, Y.; Wei, M.; Walters, G.; Wang, Z.; Zhao, Y.; Todorovic, P.; Kelley, S. O.; Chen, L. J.; Sargent, E. H. Heterogeneous Supersaturation in Mixed Perovskites. *Adv. Sci.* **2020**, *7*, 1903166 Published Online: Feb. 8, 2020.

(3) Wang, W.; Zhao, D.; Zhang, F.; Li, L.; Du, M.; Wang, C.; Yu, Y.; Huang, Q.; Zhang, M.; Li, L.; Miao, J.; Lou, Z.; Shen, G.; Fang, Y.; Yan, Y. Highly Sensitive Low-Bandgap Perovskite Photodetectors with Response from Ultraviolet to the Near-Infrared Region. *Adv. Funct. Mater.* **2017**, *27*, 1703953.

(4) Zhang, Y.; Cheng, X.; Tu, D.; Gong, Z.; Li, R.; Yang, Y.; Zheng, W.; Xu, J.; Deng, S.; Chen, X. Engineering the Bandgap and Surface Structure of CsPbCl3 Nanocrystals to Achieve Efficient Ultraviolet Luminescence. *Angew. Chem., Int. Ed. Engl.* **2021**, *60*, 9693−9698 Published Online: Mar. 10, 2021.

(5) Earn, D. J. D.; Ma, J.; Poinar, H.; Dushoff, J.; Bolker, B. M. Acceleration of plague outbreaks in the second pandemic. *Proc. Natl. Acad. Sci. U.S.A.* **2020**, *117*, 27703−27711 Published Online: Oct. 19, 2020.

(6) Francke, M.; Korevaar, M. Housing markets in a pandemic: Evidence from historical outbreaks. *J. Urban Econ.* **2021**, *123*, 103333.

(7) Ding, W.; Zhou, J.; Cheng, J.; Wang, Z.; Guo, H.; Wu, C.; Xu, S.; Wu, Z.; Xie, X.; Wang, Z. L. TriboPump: A Low-Cost, Hand-Powered Water Disinfection System. *Adv. Energy Mater.* **2019**, *9*, 1901320.
(8) Li, X.-F.; Mitch, W. A. Drinking Water Disinfection Byproducts (DBPs) and Human Health Effects: Multidisciplinary Challenges and Opportunities. *Environ. Sci. Technol.* **2018**, *52*, 1681−1689 Published Online: Jan. 21, 2018.
(9) Wang, J.; Shen, J.; Ye, D.; Yan, X.; Zhang, Y.; Yang, W.; Li, X.; Wang, J.; Zhang, L.; Pan, L. Disinfection technology of hospital wastes and wastewater: Suggestions for disinfection strategy during coronavirus Disease 2019 (COVID-19) pandemic in China. *Environ. Pollut.* **2020**, *262*, 114665 Published Online: Apr. 24, 2020.
(10) Xu, B.; Wang, H.; Wang, W.; Gao, L.; Li, S.; Pan, X.; Wang, H.; Yang, H.; Meng, X.; Wu, Q.; Zheng, L.; Chen, S.; Shi, X.; Fan, K.; Yan, X.; Liu, H. A Single-Atom Nanozyme for Wound Disinfection Applications. *Angew. Chem.* **2019**, *131*, 4965−4970.
(11) Pazoki, M.; Jacobsson, T. J.; Hagfeldt, A.; Boschloo, G.; Edvinsson, T. Effect of metal cation replacement on the electronic structure of metalorganic halide perovskites: Replacement of lead with alkaline-earth metals. *Phys. Rev. B* **2016**, *93*, 144105.
(12) Giustino, F.; Snaith, H. J. Toward Lead-Free Perovskite Solar Cells. *ACS Energy Lett.* **2016**, *1*, 1233−1240.
(13) Yang, S.; Fu, W.; Zhang, Z.; Chen, H.; Li, C.-Z. Recent advances in perovskite solar cells: efficiency, stability and lead-free perovskite. *J. Mater. Chem. A* **2017**, *5*, 11462−11482.
(14) Chen, S.; Shi, G. Two-Dimensional Materials for Halide Perovskite-Based Optoelectronic Devices. *Adv. Mater.* **2017**, *29*, 1605448 Published Online: Mar. 3, 2017.
(15) Fraccarollo, A.; Cantatore, V.; Boschetto, G.; Marchese, L.; Cossi, M. Ab initio modeling of 2D layered organohalide lead perovskites. *J. Chem. Phys.* **2016**, *144*, 164701.
(16) Gai, C.; Wang, J.; Wang, Y.; Li, J. The Low-Dimensional Three-Dimensional Tin Halide Perovskite: Film Characterization and Device Performance. *Energies* **2019**, *13*, 2.
(17) Han, X.; Zheng, Y.; Chai, S.; Chen, S.; Xu, J. 2D organic-inorganic hybrid perovskite materials for nonlinear optics. *Nanophotonics* **2020**, *9*, 1787−1810.
(18) Bartel, C. J.; Sutton, C.; Goldsmith, B. R.; Ouyang, R.; Musgrave, C. B.; Ghiringhelli, L. M.; Scheffler, M. New tolerance factor to predict the stability of perovskite oxides and halides. *Sci. Adv.* **2019**, *5*, No. eaav0693, Published Online: Feb. 8, 2019.
(19) Qiao, H. W.; Yang, S.; Wang, Y.; Chen, X.; Wen, T. Y.; Tang, L. J.; Cheng, Q.; Hou, Y.; Zhao, H.; Yang, H. G. A Gradient Heterostructure Based on Tolerance Factor in High-Performance Perovskite Solar Cells with 0.84 Fill Factor. *Adv. Mater.* **2019**, *31*, 1804217 Published Online: Nov. 28, 2018.
(20) Tan, C.-S.; Chen, H.-S.; Chiu, C.-Y.; Wu, S.-C.; Chen, L.-J.; Huang, M. H. Facet-Dependent Electrical Conductivity Properties of PbS Nanocrystals. *Chem. Mater.* **2016**, *28*, 1574−1580.
(21) Tan, C.-S.; Chen, Y.-J.; Hsia, C.-F.; Huang, M. H. Facet-Dependent Electrical Conductivity Properties of Silver Oxide Crystals. *Chem. - Asian J.* **2017**, *12*, 293−297 Published Online: Jan. 10, 2017.
(22) Tan, C.-S.; Hsu, S.-C.; Ke, W.-H.; Chen, L.-J.; Huang, M. H. Facet-dependent electrical conductivity properties of Cu2O crystals. *Nano Lett.* **2015**, *15*, 2155−2160 Published Online: Feb. 25, 2015.
(23) Tan, C.-S.; Lu, Y.-J.; Chen, C.-C.; Liu, P.-H.; Gwo, S.; Guo, G.-Y.; Chen, L.-J. Magnetic MoS 2 Interface Monolayer on a CdS Nanowire by Cation Exchange. *J. Phys. Chem. C* **2016**, *120*, 23055−23060.
(24) Togo, A.; Tanaka, I. First principles phonon calculations in materials science. *Scr. Mater.* **2015**, *108*, 1−5.
(25) Wolloch, M.; Gruner, M. E.; Keune, W.; Mohn, P.; Redinger, J.; Hofer, F.; Suess, D.; Podloucky, R.; Landers, J.; Salamon, S.; Scheibel, F.; Spoddig, D.; Witte, R.; Cuenya, B. R.; Gutfleisch, O.; Hu, M. Y.; Zhao, J.; Toellner, T.; Alp, E. E.; Siewert, M.; Entel, P.; Pentcheva, R.; Wende, H. Impact of lattice dynamics on the phase stability of metamagnetic FeRh: Bulk and thin films. *Phys. Rev. B* **2016**, *94*, 174435.
(26) Leonov, I.; Poteryaev, A. I.; Anisimov, V. I.; Vollhardt, D. Calculated phonon spectra of paramagnetic iron at the α - γ phase transition. *Phys. Rev. B: Condens. Matter Mater. Phys.* **2012**, *85*, 020401.
(27) Comin, R.; Walters, G.; Thibau, E. S.; Voznyy, O.; Lu, Z.-H.; Sargent, E. H. Structural, optical, and electronic studies of wide-bandgap lead halide perovskites. *J. Mater. Chem. C* **2015**, *3*, 8839−8843.
(28) Maculan, G.; Sheikh, A. D.; Abdelhady, A. L.; Saidaminov, M. I.; Haque, M. A.; Murali, B.; Alarousu, E.; Mohammed, O. F.; Wu, T.; Bakr, O. M. CH3NH3PbCl3 Single Crystals: Inverse Temperature Crystallization and Visible-Blind UV-Photodetector. *J. Phys. Chem. Lett.* **2015**, *6*, 3781−3786 Published Online: Sep. 17, 2015.
(29) Nandi, P.; Giri, C.; Swain, D.; Manju, U.; Topwal, D. Room temperature growth of CH 3 NH 3 PbCl 3 single crystals by solvent evaporation method. *CrystEngComm* **2019**, *21*, 656−661.
(30) Hsu, H.-P.; Li, L.-C.; Shellaiah, M.; Sun, K. W. Structural, Photophysical, and Electronic Properties of CH3NH3PbCl3 Single Crystals. *Sci. Rep.* **2019**, *9*, 13311 Published Online: Sep. 16, 2019.
(31) Kresse, G.; Hafner, J. Ab initio molecular dynamics for liquid metals. *Phys. Rev. B: Condens. Matter Mater. Phys.* **1993**, *47*, 558−561.
(32) Kresse, G.; Furthmüller, J. Efficiency of ab-initio total energy calculations for metals and semiconductors using a plane-wave basis set. *Comput. Mater. Sci.* **1996**, *6*, 15−50.
(33) Csonka, G. I.; Perdew, J. P.; Ruzsinszky, A.; Philipsen, P. H. T.; Lebègue, S.; Paier, J.; Vydrov, O. A.; Ángyán, J. G. Assessing the performance of recent density functionals for bulk solids. *Phys. Rev. B: Condens. Matter Mater. Phys.* **2009**, *79*, 155107.
(34) Becke, A. D.; Johnson, E. R. A simple effective potential for exchange. *J. Chem. Phys.* **2006**, *124*, 221101.
(35) Tran, F.; Blaha, P. Accurate band gaps of semiconductors and insulators with a semilocal exchange-correlation potential. *Phys. Rev. Lett.* **2009**, *102*, 226401 Published Online: Jun. 3, 2009.
(36) Perdew, J. P.; Burke, K.; Ernzerhof, M. Generalized Gradient Approximation Made Simple. *Phys. Rev. Lett.* **1996**, *77*, 3865−3868.

https://doi.org/10.1021/acsomega.1c06088
ACS Omega 2022, 7, 1412−1419